JPhys Energy

PURPOSE-LED PUBLISHING™

PAPER • OPEN ACCESS

Investigating charge dynamics at lead halide perovskite single crystal surfaces

To cite this article: Birgit Kammlander *et al* 2025 *J. Phys. Energy* **7** 025005

Journal of Physics: Energy

PAPER

Investigating charge dynamics at lead halide perovskite single crystal surfaces

Birgit Kammlander[1], Alberto García-Fernández[1], Sebastian Svanström[1], Erika Giangrisostomi[2], Ruslan Ovsyannikov[2], Håkan Rensmo[1,3] and Ute B Cappel[1,3,*]

[1] Division of X-ray Photon Science, Department of Physics and Astronomy, Uppsala University, Box 516, SE-751 20 Uppsala, Sweden
[2] Institute Methods and Instrumentation for Synchrotron Radiation Research, Helmholtz-Zentrum Berlin GmbH, Albert-Einstein-Straße 15, 12489 Berlin, Germany
[3] Wallenberg Initiative Materials Science for Sustainability, Department of Physics and Astronomy, Uppsala University, 751 20 Uppsala, Sweden
[*] Author to whom any correspondence should be addressed.

E-mail: ute.cappel@physics.uu.se

Keywords: lead halide perovskite, photoelectron spectroscopy, time-resolved photovoltage measurements, ion migration

Supplementary material for this article is available online

OPEN ACCESS

RECEIVED
13 September 2024

REVISED
21 December 2024

ACCEPTED FOR PUBLICATION
6 January 2025

PUBLISHED
17 January 2025

Abstract

To further develop lead halide perovskites for their application in solar cells, understanding the material's fundamental behavior under illumination is necessary. Investigating light-induced charge dynamics in single crystals can give insight into material inherent properties. Time-resolved photoelectron spectroscopy (TR-PES) allows to monitor the photovoltage build-up and decay between the sample surface and bulk over time and gives information on light-induced charge redistribution within the crystal. Additionally, this method enables us to follow compositional changes and surface degradation and distinguish these from purely electronic effects. Here we investigated the charge dynamics of two distinct lead halide perovskite single crystal surfaces ($CsPbBr_3$, Cs-doped $FAPbI_3$) using TR-PES in different timescales (ps to μs and s to min). It was found that $CsPbBr_3$ shows photovoltage rise and decay on the nanosecond to microsecond time-range, which can be assigned to electron–hole pair separation between surface and bulk. On the other hand, such electron dynamics could not be resolved for Cs-doped $FAPbI_3$ at these fast timescales. Instead, for Cs-doped $FAPbI_3$, the observed photovoltage decay was dominated by much slower dynamics and relaxation to the dark equilibrium state took around 10 min. This suggests that ion migration is responsible for a photovoltage build-up between surface and bulk of the crystal.

1. Introduction

Lead halide perovskites have been researched in-depth due to their tunable and favorable optoelectronic properties for applications such as solar cells, light emitting diodes (LEDs), photocatalysts or batteries [1–3]. Halide perovskites are represented by the general chemical formula ABX_3, where A is a monovalent cation (e.g. methylammonium/MA^+, formamidinium/FA^+, Cs^+), B is a divalent cation (typically Pb^{2+}), and X is a halide (e.g. I^-, Br^-, Cl^-). Much of the research on this class of materials is centered around multi-crystalline lead halide perovskite thin films [1, 4]. However, the use of single crystals instead of thin films as the active material in opto-electronic applications has received more attention within the scientific community due to recent performance improvements of lead halide perovskite single crystals solar cells and LEDs [5–7]. Generally, the properties of thin films made via spin-coating are less reproducible than those of single crystals, as slight changes can lead to changes in film and grain boundary formation [8]. Since recombination losses and initial degradation are known to happen predominantly at grain boundaries [4, 9], the exact film structure plays a crucial role for these applications. However, grain boundary effects can be avoided by using single crystals instead, potentially leading to better performance and stability [10]. Additionally,

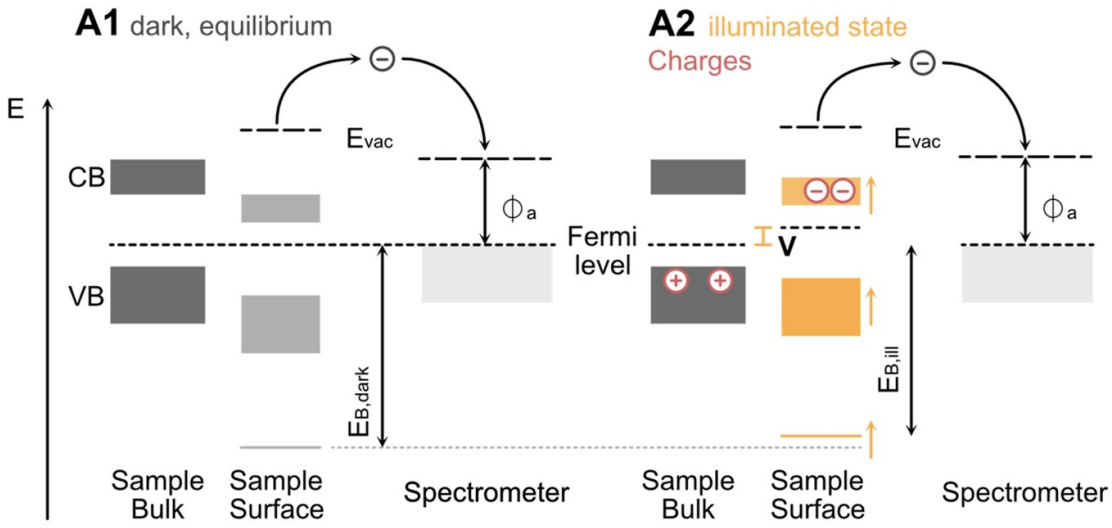

Figure 1. Schematic diagram of energy level alignment of sample (bulk, surface) and PES spectrometer at equilibrium (dark, left) and under visible light (illuminated state, right) including the photoelectron emission process for an n-type surface having a lower valence band (VB) energy of the surface in comparison to the bulk. The vacuum energy level (E_{vac}), binding energy of a particular core level under dark ($E_{B,dark}$) and illumination ($E_{B,ill}$) and the work function of the spectrometer (ϕ_a) are marked.

characterization of single crystals allows understanding inherent material properties, less affected by preparation methods [10].

Furthermore, despite lead halide perovskite solar cells achieving competitive efficiencies [11], the detailed behavior under various stressors, e.g. heat, moisture, or light, is still not fully understood [4, 12]. Particularly, fundamental understanding of the material's properties under light is necessary to further improve lead halide perovskite optoelectronic devices. Photoelectron spectroscopy (PES) can give insight into composition, compositional changes, band bending and (interfacial) energy alignment [13]. Charge transfer to transport layers and the charge movement and redistribution under illumination can be followed indirectly through determining the surface and interface photovoltage built-up within the sample with PES [14–16].

The aim of the study presented here is to demonstrate that two distinctly different mechanisms underlying charge dynamics in lead halide perovskites can be observed and investigated using time-resolved PES (TR-PES) on a wide range of timescales. Therefore, it is important to understand how PES can be used to follow photovoltages generated within investigated samples by illumination with visible light. Figure 1 compares the energy alignment between the spectrometer, the sample bulk and the sample surface in equilibrium (dark, A1) with an illuminated state (A2) for an n-type surface compared to the bulk. Here, the valence band (VB) is closer to the Fermi level in the bulk than at the surface. A p-type surface compared to the bulk is shown in case B in figure S1, where the conduction band (CB) is closer to the Fermi level in the bulk than at the surface. This difference in alignment could be due to band bending or due to a layered sample design, where the substrate material is in direct electrical contact with the spectrometer and different to the material at the sample surface [15, 17]. In equilibrium, the Fermi level of the sample bulk, surface and the analyzer are aligned [18], which is typically the case when recording PES spectra, in particular when using a low X-ray flux. As PES is a surface-sensitive technique, the specific binding energies measured for the core levels ($E_{b,dark}$) give insight into the surface region [18]. Under illumination with visible photons (e.g. laser light), the excitation of electrons from the VB to the CB is followed by a redistribution of charges, which can result in a shift of the observed VB and CB at the surface. This is often also described as a shift of the Fermi level when comparing the bulk and the surface [19]. Following that the shift is a result of electrostatic changes from the redistribution of electrons and holes, i.e. a rigid band model, the core levels will shift by the same amount as the VB [19]. Therefore, by measuring the newly distributed core level binding energy positions ($E_{b,ill}$), the photovoltage (V) changes caused by visible illumination can be followed [20]. Assuming Fermi level matching between the analyzer and the sample bulk under illumination, this photovoltage is given by the energy difference between the core level in the dark and under illumination. In figure 1 A2, illumination causes electron accumulation at the surface and therefore a core and valence level shift towards lower binding energy in comparison to the bulk and spectrometer Fermi level.

To determine energy alignment of lead halide perovskites under illumination, PES measurements have commonly focused on full or half stacks of thin film devices. Measurements comparing the dark versus

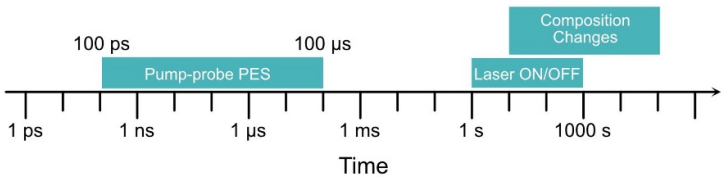

Figure 2. Illustration of the timescales of processes we can follow using PES, including pump-probe PES and laser ON/OFF measurements.

illuminated steady state have shown shifts in binding energy, which were initially attributed to surface band bending [21]. For instance, Zu *et al* found that various lead halide perovskite compositions appeared to have n-type surfaces and p-type character in the bulk, as well as shifts to lower binding energies more than 700 meV when combining UV and visible light illumination [21], which corresponds to case A2 in figure 1.

However, later studies focused on the effects of different hole transport materials above or below the perovskite layer and attributed binding energy shifts of more than 0.8 eV to charge accumulation within the perovskite at the interface to the transport material [15]. Others highlighted the importance of interface formation between the perovskite and the hole transport material, which was found to contribute substantially to the photovoltage build-up [16]. Additionally, TR-PES was used to study the charge transfer dynamics at transport material/$FAPbI_3$ nanocrystals and expected band realignment was found for the respective half-stacks within milliseconds [22].

Overall, substrate and interface effects will always impact the photovoltages observed for these half/full device stacks. To further understand the material inherent properties, studies on lead halide perovskite single crystal surfaces can be carried out. Zu *et al* compared $MAPbI_3$ single crystals with $MAPbI_xCl_{3-x}$ thin films and found n-type behavior in the dark for both samples via ultraviolet PES (UPS) [23]. However, while they observed significant shifts in binding energy in the thin film sample under illumination, the binding energy shifts in the single crystal were negligible. It is worth noting, that they did observe metallic lead from the start at the single crystal surface, which may have caused Fermi level pinning close to the CB already before illuminating the sample.

The model shown in figure 1 above only considers a redistribution of electrons and holes causing photovoltages. However, research on behavior of lead halide perovskites under illumination has shown that in addition to generating electron and hole pairs, light can induce chemical changes such as ion migration and phase separation [24–27]. The mobile ions can also cause changes in the electric field distribution in samples under illumination. When measuring only the steady-state photovoltage, it is therefore difficult to distinguish effects of electron and ion movements. However, time-resolved measurements over a large range of timescales can help to distinguish different processes and give information on their dynamics. Time-resolved studies of the photovoltage build-up and decay have been carried out on other materials [14, 28], but not on lead halide perovskite single crystal surfaces. Therefore, the inherent photovoltage rise and decay under illumination and the detailed charge dynamics of the material itself instead of half/full stack devices need to be addressed to gain fundamental understanding.

To understand charge dynamics whilst minimizing any degradation that may affect the observed photovoltage build-up and decay, preliminary experiments were carried out to find crystal compositions stable under laser light exposure and that show minimal decomposition effects. On the basis of this, the compositions $CsPbBr_3$ and Cs-doped $FAPbI_3$ were chosen for this work. The charge dynamics and stability of these two distinct single crystal compositions were then studied under illumination with visible light via synchrotron-based TR-PES on clean crystal surfaces. This allowed us to follow both electronic and compositional changes of the surfaces while excluding substrate effects due to the thickness of the crystalline samples. Additionally, this technique allowed us to follow different timescales, as illustrated in figure 2. Laser pump—X-ray probe measurements cover processes that happen within pico- to microseconds, laser ON/OFF measurements cover the second timescale and compositional changes in prolonged laser exposure experiments can be followed on timescales of seconds to minutes.

2. Experimental

2.1. Synthesis of $CsPbBr_3$ and Cs-doped $FAPbI_3$ single crystals

$CsPbBr_3$ and Cs-doped $FAPbI_3$ perovskite single crystals were synthesized using the inverse temperature crystallization method. Diameters around 0.5 cm were obtained for both crystals. The starting materials were used as bought without further treatment. Formamidinium iodide ($CH(NH_2)_2I$, FAI), cesium iodide (CsI),

Table 1. Reagents used for single crystal synthesis.

Full chemical name	Chemical formula/ abbreviation	Supplier	Purity
Formamidinium iodide (FAI)	$CH(NH_2)_2I$	Sigma Aldrich	Assay ⩾98%
Cesium iodide	CsI	Sigma Aldrich	99.9%
Cesium bromide	CsBr	Sigma Aldrich	99.999%
Lead iodide	PbI_2	TCI	>98.0%
Lead bromide	$PbBr_2$	Sigma Aldrich	99.999%
γ-butyrolactone	GBL	Sigma Aldrich	⩾99.0%
Dimethylsulfoxide	DMSO	Sigma Aldrich	⩾99.9%

cesium bromide (CsBr) and lead bromide ($PbBr_2$) were purchased at Sigma Aldrich. Lead iodide (PbI_2) was purchased at TCI. Details on all reagents used can be found in table 1.

For Cs-doped $FAPbI_3$ perovskite single crystals, a 1 M 1:1 FAI:PbI_2 solution was prepared using γ-butyrolactone (GBL). When the precursors were completely dissolved, 0.1 M of CsI was added. The mixture was stirred at room temperature until a yellow transparent solution was obtained. For $CsPbBr_3$, CsBr and $PbBr_2$ were dissolved on DMSO in a molar ratio of 1:2, leading to the formation of a transparent saturated perovskite precursor solution.

Both solutions were filtered through a 0.45 μm PTFE filter, transferred to an open glass vial and heated to 100 °C (Cs-doped $FAPbI_3$) and 120 °C ($CsPbBr_3$). After 1–2 h selected seed crystals were collected. New glass vials containing filtered mother solution were again heated up to 100 °C for Cs-doped $FAPbI_3$ and 120 °C for $CsPbBr_3$. Once the desired temperature was reached, selected seed crystals were introduced into the new solution and allowed to grow with the vial sealed until the desired crystal size was achieved.

The most suitable crystals were chosen for characterization using PES. The remaining ones from the same batch were characterized by powder X-ray diffraction analysis. Supplementary figure S2 shows a comparison between the powder XRD and the single crystal XRD profiles from literature. All the synthesized materials show a single phase, free from any impurities. An orthorhombic crystal structure was found for $CsPbBr_3$. After addition of small amounts of cesium the cubic phase of $FAPbI_3$ could be stabilized. The amount of Cs in the Cs-doped $FAPbI_3$ crystal was estimated to be approximately 3% relative to FA and Pb. Quantification of the Cs 4d and C 1s core level spectra accounting for the difference in inelastic mean free path (IMFP) and cross sections gave a value of 3.4% of cesium. Quantification from the Cs 4d:Pb 4f ratio of Cs-doped $FAPbI_3$ relative to Cs 4d:Pb 4f ratio of $CsPbBr_3$ (assumed to be 1:1) gave a value of 2.6%. The uncertainty in this quantification is relatively high due to the small amount of cesium at the surface. Overall, the calculation shows that cesium is present but in a lower amount than added in the synthesis.

2.2. TR-PES

The PES measurements were carried out at the LowDosePES end-station at the PM4 beamline at the BESSY II synchrotron facility (Helmholtz-Zentrum Berlin, HZB, Germany) [29, 30]. The beamline was operated in quasi-single bunch mode, using a mechanical chopper to isolate a single bunch of 4 mA nominal current, an X-ray pulse frequency of 1.25 MHz and an x-ray pulse length of ∼70 ps full width half maximum. The X-rays were monochromatized using a plane grating monochromator with a 360 l mm^{-1} grating. The pressure in the analysis chamber was sub 10^{-9} mbar and the measurements were carried out at ambient temperature. The photoelectrons were detected using an angular-resolved time-of-flight (ArTOF) spectrometer with an acceptance cone of ±15° for high photoelectron transmission.

For the TR-PES measurements the second harmonic (515 nm) of a pump laser (Tangerine, Amplitude Systèmes) with a pulse length of ∼350 fs was used. The time between two laser pulses was set to 96 μs by using a repetition frequency of 10.4 kHz. The time overlap between x-ray and laser pulses was checked using the arrival times of both x-ray and laser photons measured by the ArTOF spectrometer. The laser delay was then electronically set relative to the incident X-ray pulses throughout the experiment. The laser power was set to 0.05 mW via filters, which equals 4.8 nJ per pulse. The spatial alignment of the incident X-rays and laser pulses was checked by letting the beams impinge, one at a time, on a luminescent sample and comparing microscope camera images. The X-ray and laser beams spot were an ellipse due to the 45° incident angle. 2D-Gaussian fitting of the intensity profiles of the camera images was used to estimate the laser spot size. The standard deviation of the Gaussian profile was 0.098 mm vertically and 0.102 mm horizontally. Using the standard deviation, 68% of the laser power (0.034 mW/3.3 nJ/pulse) is incident in an area of 0.031 mm^2. Therefore, the laser fluence is 10.4 μJ cm^{-2} and the laser power density is equal to 108 mW cm^{-2}. The laser photon flux per area was estimated to about 2.8×10^{17} photons s^{-1} cm^{-2}. These laser settings were used for all measurements. The X-ray spot size (standard deviation) was estimated to 0.080 mm vertically and

0.073 mm horizontally. Therefore, 68% of the X-rays are incident in an area of 0.018 mm^2. The X-ray flux is in the order of 10^7 photons s^{-1} [29], i.e. between 10^{10} and 10^{11} photons s^{-1} cm^{-2}.

All pump-probe measurements (delay scans) were carried out on fresh sample spots with a photon energy of 90 eV. The single crystals were cleaved under vacuum conditions to obtain a clean surface. To ensure clean surfaces, the spots were briefly checked for the absence of adventitious carbon via C 1s core level spectra prior to the measurements. The delay scans were carried out using a multiscan function, which allowed to measure the desired core level (Pb 5d) consecutively in fixed mode with different laser delay times, called delay points. The laser pulses were timed relative to the first incoming X-ray pulse of each delay point. 120 spectra were recorded between two laser pulses; therefore, each delay point consists of 120 spectra. The laser delay time was varied between 100 ps and 400 ns with exponentially increasing step, e.g. equal spacing between the delay times on a logarithmic time axis.

The recorded spectra were fitted via Gaussian functions to obtain peak positions for each spectrum of each delay point. Further details on the experimental set-up and the data analysis protocol can be found in a previous report on the method [28]. Supplementary figures S3 and S4 show the obtained absolute binding energies (E_b) as a function of time for $CsPbBr_3$ and Cs-doped $FAPbI_3$, respectively. To determine the binding energy change (ΔE_b), as shown in supplementary figures S5 and S6, the binding energy at the longest delay time was subtracted from all binding energy positions for each delay time. The binding energy change was then averaged as follows. At shorter timescales (<800 ns), the peak positions were used as obtained, while the obtained peak positions were averaged for the different delay times at larger timescales (>800 ns). Within the shorter timescales (<800 ns), the error range was estimated via standard deviations of measurements at different delay points at long delay times. The error range for averaged delay times at larger timescales (>800 ns) was estimated as the error in the mean using the standard deviation. Deviations greater than 5 meV are depicted as error bars. To obtain averaged, absolute binding energies, the average binding energy at long delay times was added to the averaged binding energy change. The photovoltage as a function of time was obtained by subtracting the averaged, dark binding energy (before and after the pump-probe measurements) from the averaged, absolute binding energies.

To obtain photovoltage decays on longer timescales, laser ON/OFF measurements were carried out on one core level (Pb 5d) at 90 eV photon energy. The laser settings were used as described above. For these measurements, spectra were recorded (1 spectrum per second) without laser for 180 s, followed by measurements with the laser ON for 120 s. This cycle was repeated six times, ending with one laser OFF cycle for $CsPbBr_3$. For Cs-doped $FAPbI_3$ only 4 ON/OFF cycles were done, with the remaining experiment time measuring under laser OFF condition to follow full relaxation of the system. The first laser OFF and ON spectra of each composition are shown in supplementary figure S7, the evolution of the spectra over time as a 2D image in supplementary figure S8.

Furthermore, the stability towards X-rays and laser was investigated with prolonged measurements. The laser settings are described above. For these, relevant core levels for the given composition were measured (Pb 4f, Cs 4d, Br 3d, I 4d, C 1s) at 363 eV photon energy. The spectra were recorded in loops without laser for 36 min, followed by measurements with the laser ON for 24 min. This cycle was repeated four times, ending with one laser OFF cycle. The spectral evolution is shown in supplementary figures S9 and S10 for $CsPbBr_3$ and Cs-doped $FAPbI_3$, respectively.

The laser ON/OFF measurements and the stability measurements were fitted using pseudo-Voigt functions with linear or Shirley background [31], as needed.

All spectra were energy calibrated either towards Au $4f_{7/2}$ at 84.0 eV or the Fermi level measured on a gold reference mounted on the sample plate, as specified. Intensity normalization was done against Pb 4f for the stability measurements.

The IMFP was calculated using the TPP-2M method [32], as specified in the supplementary information and supplementary table S1. The IMFP varies between 0.48 and 1.02 nm, depending on the exact core level, composition, and photon energy.

3. Results

In this study, the charge carrier dynamics at timescales between picoseconds (ps) and seconds (s) of two clean single crystal surfaces ($CsPbBr_3$ and Cs-doped $FAPbI_3$) were investigated. The crystals were grown in-house and cleaved under ultra-high vacuum conditions to obtain clean surfaces [33–36], followed by probing the materials via (TR-)PES without breaking vacuum at the LowDosePES endstation at Bessy II (Berlin). A general characterization of the clean surfaces was carried out at 363 eV photon energy, where the core levels Pb 4f, C 1s, Cs 4d, Br 3d and I 4d were recorded. Additionally, the VB was recorded at 90 eV photon energy (see supplementary figure S10). The measurements show the core levels expected for the given sample compositions [33, 36]. For Cs-doped $FAPbI_3$, the Cs 4d signal was low and difficult to quantify

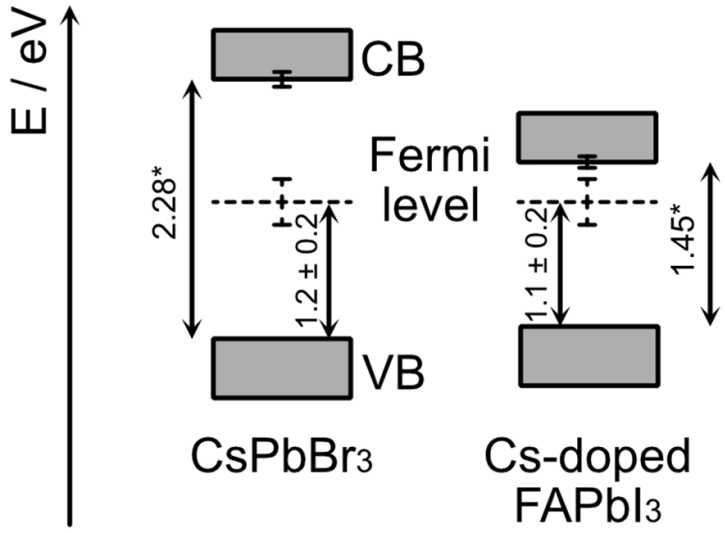

Figure 3. Energy alignment of both crystal compositions, including determined valence band edge with error ranges and literature band gap values. *Literature band gap values vary considerably. For $CsPbBr_3$ values between 2.21 and 2.34 eV [38–40] and for Cs-doped $FAPbI_3$ values between 1.4 and 1.49 eV [37, 38] are reported. For simplification, the average value of the literature values was used.

accurately. Quantification was carried out on an average of multiple spectra (see supplementary figure S12 and Experimental section) and about 3% Cs were found in Cs-doped $FAPbI_3$. Furthermore, no metallic lead (Pb^0) was observed for either crystal surface. Additionally, the VB edge of both crystal compositions was estimated (see figure S13) to be 1.1 ± 0.2 eV and 1.2 ± 0.2 eV for Cs-doped $FAPbI_3$ and $CsPbBr_3$, respectively, in agreement with previous results [33]. The reported band gap ranges between 1.4 and 1.49 eV [37, 38] for Cs-doped $FAPbI_3$ and between 2.21 and 2.34 eV [38–40] for $CsPbBr_3$. This indicates that both crystals are n-type at the surface as the Fermi level is closer to the conduction than to the VB, as shown in figure 3. Notably, the $CsPbBr_3$ surface is only slightly n-type. Most studies on the surface band bending of lead halide perovskites center around thin films [41, 42], where the underlying substrate can impact the overall energy alignment [15]. Specifically, lead halide perovskite thin films on top of n-type TiO_2 typically have an n-type surface [43]. However, due to the thickness of the single crystals here, substrate effects can be excluded for our results. It is worth noting that others have reported a p-type surface for monoclinic $CsPbBr_3$ single crystals via UPS [44]. However, we are investigating orthorhombic $CsPbBr_3$ single crystals in the work presented here (see Experimental), which may affect surface properties.

Two types of time-resolved measurements (reported below) were carried out on the surfaces to access processes on different time scales: laser pump—X-ray probe PES measurements to follow the charge dynamics in the picosecond to microsecond (ps to μs) time range and longer laser ON/OFF cycles (180 s OFF/120 s ON or 36 min OFF/24 min ON) to follow the slower timescales and the surface composition over time. The laser ON/OFF cycles at seconds timescale were optimized for the Pb 5d core level, where the measurement frequency was one spectrum/second at 90 eV photon energy. To also follow compositional changes, all relevant core levels were recorded at a higher photon energy of 363 eV and the laser exposure was prolonged. New, clean spots were used for each of those measurements. The same pulsed laser with a photon energy of 2.41 eV and a repetition rate of 10.4 kHz was used for all experiments. Notably, the overall laser power density was relatively similar to the standard power density of 1 sun with the used settings. In comparison, the X-ray flux is much lower and not expected to cause much band to band excitation (see Experimental). We have shown this also in a complete quantum dot solar cell with similar settings, where the laser generates shifts of up to 0.67 eV, while X-rays caused shifts of less than 0.03 eV [45]. We can therefore assume that the Fermi level at the surface is aligned with the spectrometer under X-ray illumination. In the sections below, the focus will be on the charge dynamics in the faster timescales (ps to μs) first, followed by discussing slower timescales (s to min) and stability behavior.

3.1. Time-resolved photovoltage

By using pulsed laser and X-ray sources, it is possible to follow the change in binding energy (and therefore photovoltage) as a function of time. In figure 4, the photovoltage build-up and decay as a function of delay time for the $CsPbBr_3$ (blue) and the Cs-doped $FAPbI_3$ (pink) surface is shown, as determined via curve fitting of Pb 5d core levels of different X-ray pulses and at different laser delay times relative to the first X-ray pulse.

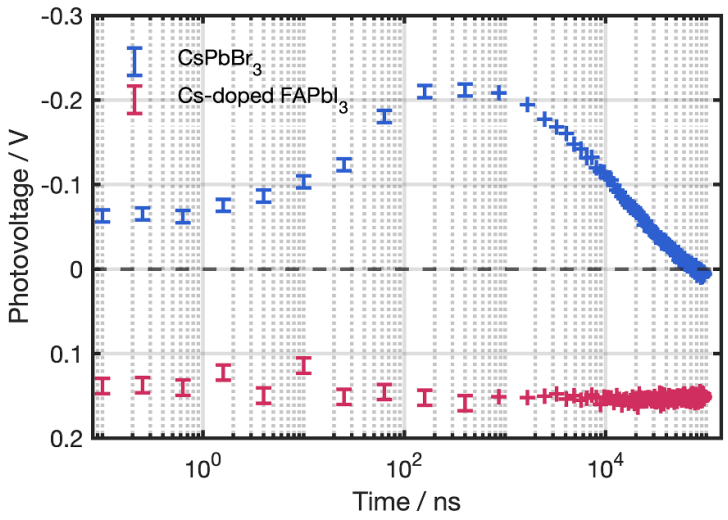

Figure 4. Kinetic traces of photovoltage built-up and decay of $CsPbBr_3$ (blue) and Cs-doped $FAPbI_3$ (pink) determined via binding energy changes from delay scans measured at 90 eV photon energy.

Details can be found in the Experimental section. It is important to note, that we are following the change in charge distributions in the crystals by probing the surfaces of the samples, as described in the introduction. Firstly, the magnitude of the observed maximum photovoltage is larger for $CsPbBr_3$ than for Cs-doped $FAPbI_3$, see figure 4. Furthermore, the two samples show opposite signs of their photovoltage. For $CsPbBr_3$ the core levels shift to a lower binding energy under illumination (shown as a negative photovoltage), while for Cs-doped $FAPbI_3$ the core levels shift to a higher binding energy (shown as a positive photovoltage). Considering only electronic changes, e.g. moving electrons and holes, the opposite shifts in binding energy may be attributed to different band bending towards the surface of the two crystal compositions. This would suggest that $CsPbBr_3$ exhibits a more n-type surface than bulk while Cs-doped $FAPbI_3$ has more p-type character at the surface than bulk (see figure 1). However, our estimation of the VB edge in combination with the band gap (see figure 3) revealed a more n-type surface for Cs-doped $FAPbI_3$ than for $CsPbBr_3$.

Furthermore, the time-dependence of the photovoltage for each crystal surface varies. For Cs-doped $FAPbI_3$, the photovoltage remains at approximately the same positive value throughout the probed timescale, indicating that the system does not relax between two laser pulses. In other words, the laser repetition frequency is too high for this system, as the photovoltage cannot decay with the chosen settings. Instead, the observed photovoltage is the result of a steady-state obtained during the illumination with laser pulses with a repetition frequency of 10.4 kHz. In contrast, the chosen experimental settings allow us to follow the dynamics of charge redistribution in $CsPbBr_3$, as a clear photovoltage build-up and decay is observed.

To also follow the dynamics of Cs-doped $FAPbI_3$, the photovoltage decay on slower time scales was investigated by cycling laser ON/OFF measurements. With optimized experimental settings, Pb 5d core level spectra could be analyzed with a rate of 1 Hz. Figure 5 shows the change in binding energy under cycled laser ON/OFF conditions as a function of time for $CsPbBr_3$ (left) and Cs-doped $FAPbI_3$ (right). The change in binding energy positions was obtained via curve fitting the measured Pb 5d core levels and calculating the shift in binding energy position for all core level spectra relative to the first spectrum. The two crystals show distinct behavior with $CsPbBr_3$ shifting to lower binding energy and Cs-doped $FAPbI_3$ shifting to higher binding energy under illumination, in agreement with the results presented in figure 4. Our results for $CsPbBr_3$ are furthermore in agreement with a study by Polishchuk *et al* who also observed a shift to lower binding energies under illumination for $CsPbBr_3$ single crystals via time-resolved angular resolved PES [46].

After the first laser ON/laser OFF cycle, the new binding energy position in the dark of the $CsPbBr_3$ core levels is at higher binding energy position than initially. A similar change to the binding energy position in the dark is observed before and after delay scans (supplementary figures S3 and S4). The binding energy positions under dark conditions remain constant in the subsequent laser ON/OFF cycles, indicating a more permanent change of the sample surface induced by the first illumination. Additionally, a slow drift towards less negative binding energy shifts is observed under laser ON, and a slow drift towards less positive binding energy shifts under laser OFF, i.e. the laser ON/OFF contrast tends to slightly decrease over repeated illumination cycles.

Cs-doped $FAPbI_3$ slowly recovers towards the original, dark binding energy positions under its laser OFF cycles. Notably, the Cs-doped $FAPbI_3$ crystal does not fully recover within the 180 s laser OFF cycles. To

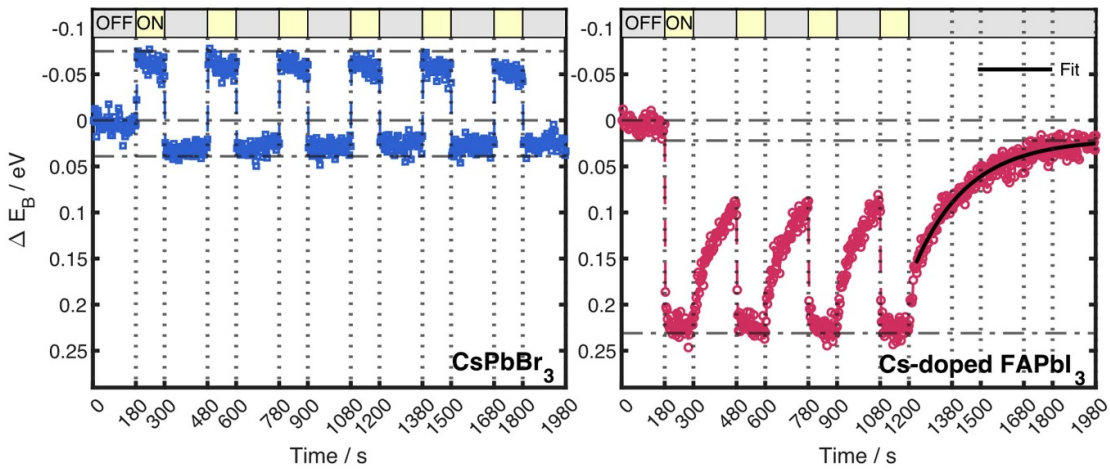

Figure 5. Pb 5d core level peak binding energy position change (ΔE_B) relative to the first peak position as a function of time during laser ON/laser OFF cycles. Core level spectra were recorded at a photon energy of 90 eV. Left: $CsPbBr_3$, 6 cycles of laser OFF (180 s)/laser ON (120 s), ending with laser OFF (180 s). Right: Cs-doped $FAPbI_3$, 4 cycles of laser OFF (180 s)/laser ON (120 s), finishing with laser OFF (780 s). The last laser OFF cycle was fitted using an exponential function, as shown as a black, solid line.

observe the full recovery dynamics at this crystal surface, the last laser OFF cycle was prolonged to 780 s. A time constant of 225 s was determined for that laser OFF cycle using an exponential fit. This laser ON/OFF behavior of Cs-doped $FAPbI_3$ contrasts the recovery observed for $CsPbBr_3$. Since $CsPbBr_3$ recovered after 100 μs in the pulsed laser measurements (see figure 4) an instantaneous recovery at longer timescales is expected, as observed in figure 5. Notably, the system stabilizes at slightly higher binding energy position compared to the initial pre-illumination state, indicating a change after illumination. Therefore, both crystal surfaces seem to have undergone some irreversible chemical or electronic changes during their exposure to the laser light, which will be discussed in further detail below. Generally, irreversible changes after illumination in vacuum have been reported previously for lead halide perovskite thin film samples, with the magnitude of the change depending on the laser light intensity and on the perovskite composition [47, 48].

3.2. Compositional changes under extended laser and x-ray exposure

To investigate the chemical stability of the samples under laser light, possibly affected by ion movement, we measured much longer laser ON/OFF cycles for both sample surfaces with a higher photon energy and including several core levels (Pb 4f, Br 3d/I 4d, Cs 4d/C 1s). Figure 6 (top) shows the change in binding energy under cycled laser ON/OFF conditions as a function of time for $CsPbBr_3$ (left) and Cs-doped $FAPbI_3$ (right). The change in binding energy positions was obtained via curve fitting the measured core levels and all core level positions were set relative to the binding energy position of the initially measured core level position, respectively. Firstly, the shifts in binding energy position under laser ON versus OFF are similar to the ones observed in figure 5. However, both compositions show additionally an overall shift after the first illumination cycle independent of the laser light exposure, i.e. the shift is present both under laser ON and laser OFF condition. For $CsPbBr_3$, an overall shift towards higher binding energies is observed, while Cs-doped $FAPbI_3$ shifts overall to lower binding energies over time. Additionally, while the core level shifts of I 4d and Pb 4f overlap in Cs-doped $FAPbI_3$, C 1s shifts overall more. In $CsPbBr_3$, the core level shifts of the different components diverge, with Cs 4d shifting significantly more than Br 3d and the latter more than Pb 4f. Overall, the shifts in binding energy positions suggest chemical changes for longer X-ray and laser exposure, as further shown in figure 6 (bottom).

In figure 6 (bottom), the change of the A-site cation (cesium, carbon) and of the halide (bromide or iodide) intensities are shown relative to the lead intensity and normalized to the ratio expected from stoichiometry. The cesium content is shown only for $CsPbBr_3$, due to only small amounts of cesium at the Cs-doped $FAPbI_3$ surface (figure S12). The spectral evolution of these core levels can be found in the supplementary information (supplementary figures S9 and S10). It is worth noting that the error range is larger for the carbon fits due to comparatively small signal to noise ratio.

Both crystal compositions show an increase in their A-site cation and halide content relative to lead at the surface over time. It is worth noting, that the compositional changes only start during the first laser ON cycle for $CsPbBr_3$, showing that the X-ray intensities used in these experiments alone do not lead to changes of the sample surface. Furthermore, while $CsPbBr_3$ increases to approximately 3.16 and 1.13 in its bromide and cesium content relative to lead, respectively, the relative iodide and carbon content increase to 3.34 and 1.36

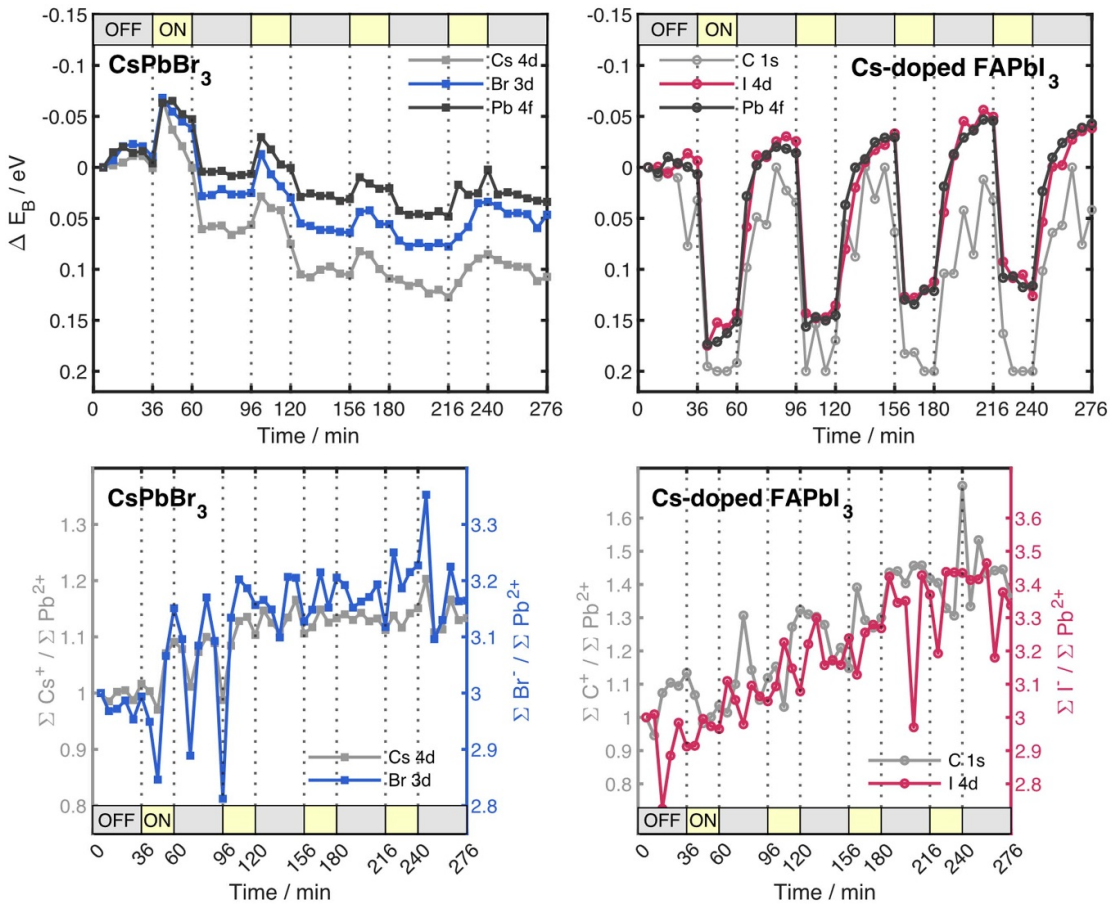

Figure 6. Top: core level binding energy shift relative to the first peak position of the timeseries as a function of time under laser ON versus OFF for $CsPbBr_3$ (left) and Cs-doped $FAPbI_3$ (right) determined from core level spectra recorded at a photon energy of 363 eV. 4 cycles laser OFF (6 sweeps, 36 min)/ON (4 sweeps, 24 min) , ending with laser OFF (6 sweeps, 36 min) of the binding energy shift of monovalent cation (Cs 4d and C 1s, light grey), halide (Br 3d in blue, I 4d in pink) and Pb 4f (black) are shown. Bottom: compositional changes of the $CsPbBr_3$ (left) and Cs-doped $FAPbI_3$ (right) surface relative to Pb 4f determined from the same core level spectra under long laser ON/OFF cycles. Intensity ratios for the first iteration were set to 1 and 3 for the cation and halide, respectively.

for Cs-doped $FAPbI_3$, respectively. These results suggest ion migration within these samples that lead to bromide and cesium rich regions at the $CsPbBr_3$ surface and iodide and FA rich regions at the Cs-doped $FAPbI_3$ surface. In contrast to our results on single crystals, Kim *et al* studied photo-induced ion migration in $FAPbI_3$ thin films via scanning electron microscopy coupled with energy-dispersive X-ray spectroscopy and found a depletion of iodide ions and an increase in lead concentration at the surface under illumination [27].

Furthermore, the 1:1 increase in cesium and bromide content relative to lead could indicate the formation of CsBr, as observed in our previous studies on X-ray degradation [36, 49]. However, we do not observe new contributions at higher binding energies or peak broadening for the Cs 4d and Br 3d core levels. Instead, we suggest that the light in combination with X-rays induces movement of cesium and bromide ions towards the surface. Since both cesium and bromide increase very similarly, no net charge built up is expected at the surface of $CsPbBr_3$ at long laser and X-ray exposure. In Cs-doped $FAPbI_3$, the A-site cation and iodide increase in a 1:1 ratio as well, indicating no net charge built up at this surface at long laser and X-ray exposure either. Notably, both cations and halides are mobile under illumination for both crystal compositions. However, the results suggest that substantially larger amounts of the cation and halide accumulate at the Cs-doped $FAPbI_3$ surface than at the $CsPbBr_3$ surface, indicating higher ion mobility in Cs-doped $FAPbI_3$. Specifically, Cs 4d and Br 3d core level intensities increased by 13.0% and 5.2%, respectively, for $CsPbBr_3$ while C 1s and I 4d core level intensities increased by 44.2% and 11.8%, respectively, for Cs-doped $FAPbI_3$.

Additionally, small amounts of Pb^0 of up to 2.4% formed at the $CsPbBr_3$ surface (see supplementary figure S14), which was also observed in our previous studies on X-ray stability of $CsPbBr_3$ single crystal [36] and thin film surfaces [49]. In comparison, no Pb^0 was observed at the Cs-doped $FAPbI_3$ surface, in agreement with our X-ray degradation study on $Cs_{0.17}FA_{0.83}PbI_3$ thin films [36]. In contrast, a study on Cs-doped $FAPbI_3$ thin films comparing degradation under red and blue laser light reported Pb^0 formation

on these surfaces [50]. However, the thin films were heated (69 °C) and exposed to much higher laser power density of 10 suns (1000 mW cm^{-2}), which could contribute to the observed degradation.

4. Discussion

The two crystal compositions shift in opposite directions under illumination, both on shorter picosecond to microsecond (figure 4) and on longer second to minute (figure 5) timescales. Considering figure 1, the shift to lower binding energy observed in $CsPbBr_3$ suggests a net negative charge accumulation, while the shift to higher binding energy observed in Cs-doped $FAPbI_3$ suggests a net positive charge accumulation at the surface under illumination.

As $CsPbBr_3$ shows overall fast charge dynamics, considering mostly electronic charge redistribution is reasonable, i.e. ion migration does not contribute substantially to the observed dynamics. Therefore, the shift to lower binding energies suggests a process that could be modeled as downwards band bending under dark conditions, i.e. that the surface is more n-type than the bulk. Under illumination, electrons in $CsPbBr_3$ accumulate at the surface, while holes move towards the bulk (see figure 7, top).

Conversely, Cs-doped $FAPbI_3$ shows a shift to higher binding energy, suggesting accumulation of positive charges at the surface under illumination. As shown in figures 4 and 5, the dynamics observed for Cs-doped $FAPbI_3$ are very slow in comparison to the $CsPbBr_3$ crystal surface. Specifically, full photovoltage decay is only reached after 10 min for Cs-doped $FAPbI_3$, while it is reached after 100 microseconds for $CsPbBr_3$. Large variations in carrier lifetimes have been observed for lead halide perovskite single crystals [38]. However, as electron and hole dynamics are typically in the order of nano- to microseconds [51], electronic changes alone seem unreasonable for explaining the observed effects in the Cs-doped $FAPbI_3$ crystal surface. Instead, additional processes must be involved in the observed dynamics. Ion migration is a well-known phenomenon reported for different lead halide perovskite thin films and single crystals [25, 27, 52–55], which could lead to very slow recovery times after illumination.

As indicated by the surface restructuring occurring upon laser illumination discussed above, mobile ions are clearly present in both crystals. It is worth noting that DFT calculations have shown lower activation energy for I^- vacancies than Br^- or Cl^- vacancies in cubic $CsPbX_3$ [56]. If ion migration leads to a change in charge distribution between the surface and bulk, it would impact the binding energy positions measured under illumination. Considering the slow timescale of the photovoltage recovery, cation or halide vacancy movement and accumulation at the surface at steady-state seems reasonable.

Overall, we can therefore propose two different mechanisms for the observed photovoltage dynamics for the two different crystal surfaces, as illustrated in figure 7. Firstly, the VB measurements indicate an n-type surface for both crystals (see figure 3 and supplementary figure S11), with Cs-doped $FAPbI_3$ exhibiting a more pronounced n-type surface character than $CsPbBr_3$. Notably, an intrinsic semiconductor without much doping is often assumed for single crystals [38], suggesting that both single crystals show downward band banding towards the surface (figure 7).

Considering both the kinetic traces of the photovoltage build-up and decay at fast timescales (figure 4) and the change in binding energies at slower timescales (figure 5) at the $CsPbBr_3$ surface, a significant impact of ion movement on the binding energy changes is unlikely at these two timescales (ps to μs and s to min), despite slight indication of slow ion movement at longer timescales (figure 5). Assigning the photovoltage to electronic movements alone, the sample shows downward band bending to a slightly n-type surface in the dark. Following laser illumination, electrons accumulate at the surface and holes move towards bulk, leading to decreased band bending at the crystal surface measured as a core level shift to lower binding energies (see figure 7, top). Eventually, a maximum photovoltage within the sample is reached, followed by electron hole recombination and a relaxation to the ground state.

Considering only electronic processes, a time constant for electron hole recombination can be determined for $CsPbBr_3$ from the photovoltage decay in figure 4. Bröcker *et al* have studied the charge carrier dynamics of SiO_2/Si (1 0 0) interfaces using TR-PES and proposed a model for photovoltage dynamics [14]. The model assumes that laser illumination causes additional charge carriers compared to the dark equilibrium state, which leads to a change in the surface potential due to their redistribution, e.g. decrease in band bending. This is followed by charge carrier recombination, leading to a decay of the photovoltage. Notably, it is assumed that recombination is predominantly limited by holes overcoming the band bending induced barrier to the surface. The model allows us to determine the recombination time in the dark (τ), which refers to the charge carrier lifetime at zero photovoltage, i.e. when ground state band bending is reached. This recombination time does not depend on the photovoltage, but on the temperature and band bending. It should, therefore, be constant for a given sample if no temperature change is induced by the laser light. We have used the following equation based on this model to fit the photovoltage decay for the kinetic

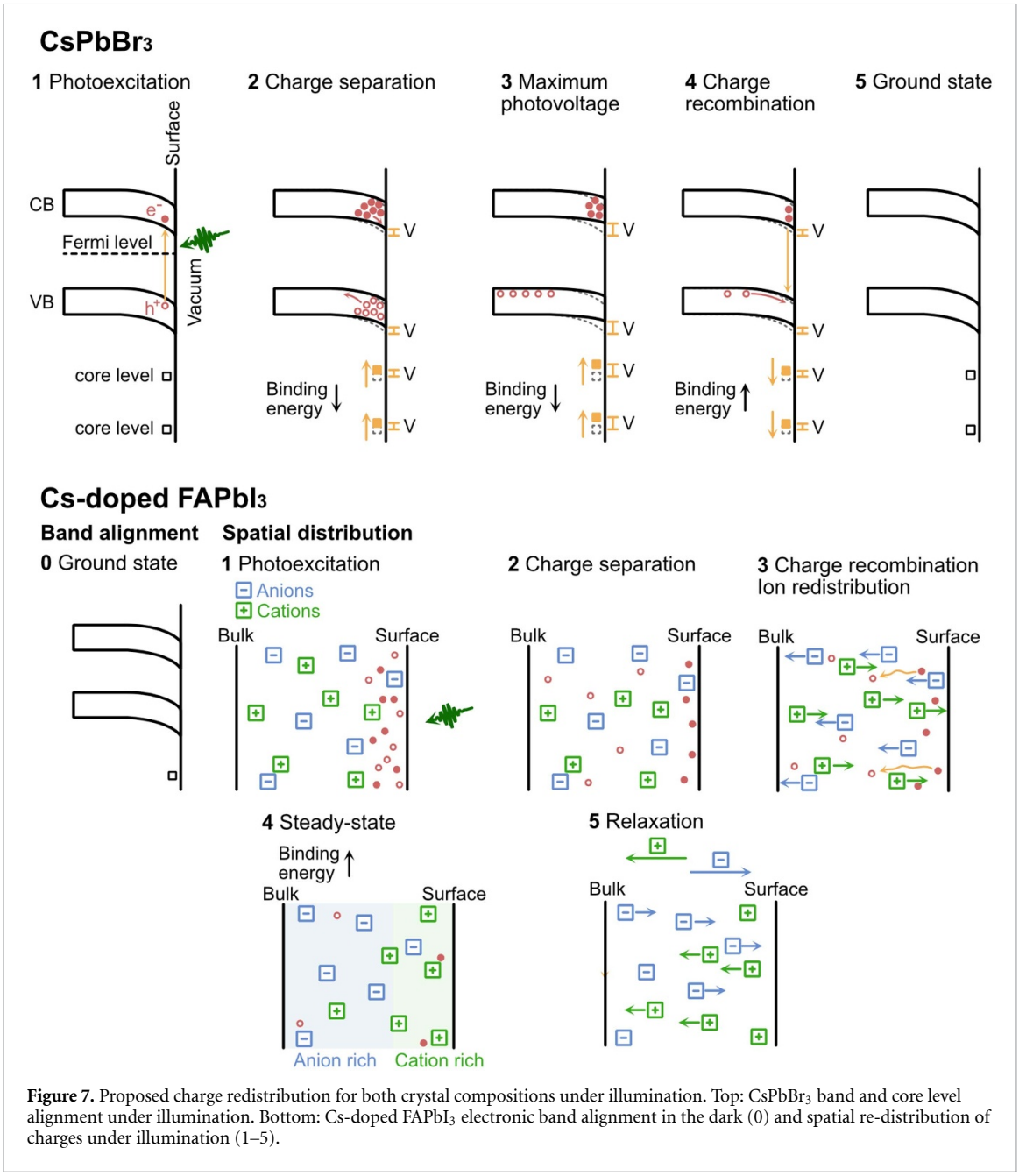

Figure 7. Proposed charge redistribution for both crystal compositions under illumination. Top: $CsPbBr_3$ band and core level alignment under illumination. Bottom: Cs-doped $FAPbI_3$ electronic band alignment in the dark (0) and spatial re-distribution of charges under illumination (1–5).

traces on a binding energy scale:

$$E_{\mathrm{b,ill}}(t)/e = -\alpha k_{\mathrm{B}} T * \log\left[1 - \left(1 - e^{\frac{-V_{\max}}{\alpha k_{\mathrm{B}} T}}\right) * e^{\frac{-t}{\tau}}\right] + E_{\mathrm{b,dark}}/e \quad (1)$$

where $E_{\mathrm{b,ill}}$ is the binding energy position under illumination, e is the charge of an electron, α is a material constant, k_{B} is Boltzman's constant, T is the temperature (298.15 K), $V_{\max}$ is the maximum surface photovoltage, t is the time, τ the recombination time in the dark and $E_{\mathrm{b,dark}}$ is the binding energy position under dark conditions (see supplementary information for details of the fitting procedure). From the fit, τ was determined to be 56.3 μs, α 3.09, $V_{\max}$ 0.27 V and $E_{\mathrm{b,dark}}$ 19.53 eV for the $CsPbBr_3$ surface (see supplementary figure S15 and supplementary table S2).

Most studies on charge carrier dynamics in perovskites use time-resolved photoluminescence (TR-PL) measurements [57, 58] rather than TR-PES. Typically, (multiple) exponential decay functions are used to retrieve charge carrier lifetimes from these measurements, which are determined by measuring the fluorescence or phosphorescence photons that are emitted when charge carriers recombine. However, fitting our data to such functions would not lead to directly comparable lifetimes, as the photovoltage is not directly proportional to the charge carrier concentration. In other words, lifetimes studied via TR-PL and TR-PES are not directly comparable.

Instead, the recombination time determined via TR-PES is expected to be longer than the charge carrier lifetime determined via TR-PL. Indeed, $CsPbBr_3$ single crystals were found to have a surface charge carrier lifetime of 1.9 ns and a bulk charge carrier lifetime of 6.8 ns [51]. In contrast, a hole carrier lifetime of 25 μs was found for $CsPbBr_3$ single crystals employed as γ-ray detectors [59]. Furthermore, decay times of 6.6 μs for n-type silicon samples and oxygen concentration dependent decay times of hundreds of μs up to 1.2 ms for n-type zinc oxide (ZnO) samples have been reported via TR-PES [20]. Compared to our results, both the indirect band gap material silicon and, even more so, the direct band gap material ZnO have shown similar photovoltage recombination times in the dark in the μs regime, indicating that comparable processes took place, i.e. predominately recombination of electronic changes.

Moving on to Cs-doped $FAPbI_3$ and assuming an intrinsic semiconductor in the bulk, Cs-doped $FAPbI_3$ is expected to have stronger downwards band bending towards the surface than $CsPbBr_3$ (figure 7, bottom panel 1). Accordingly, illumination is expected to lead to electron accumulation at the surface and hole movement towards the bulk, similar to $CsPbBr_3$ (figure 7, top). However, a corresponding shift to higher binding energies cannot be resolved at short timescales due to being masked by the slow dynamics of ion movement. As discussed above, the slow recovery of the binding energy in the dark Cs-doped $FAPbI_3$ surface after illumination (figure 5) cannot stem from electronic charge redistribution alone, as electron and hole lifetimes are typically in the order of tens to hundreds of ns, up to μs time range for lead halide perovskites [38, 60, 61]. Instead, ion movement contributes to the dynamics, which is supported by the results on prolonged laser and X-ray exposure, suggesting higher ion mobility for the Cs-doped $FAPbI_3$ surface compared to the $CsPbBr_3$ surface (figure 6).

In this case, the laser pulse train illuminates the system, exciting electrons to the CB and leaving behind holes (figure 7, bottom). At the same time, a certain number of electron–hole pairs will recombine between two laser pulses. Eventually, a state under laser illumination is reached, in which recombination of electron–hole pairs matches the amount of newly excited electrons. As electrons will accumulate at the surface and holes will move towards the bulk (figure 7, bottom panel 2), the electric field between the sample surface and the sample bulk is changed, which can induce ion redistribution. Positive ions (e.g. FA^+ interstitials or I^- vacancies) would start accumulating at the crystal surface (figure 7, bottom panel 3), essentially changing the surface potential. Photoelectrons would escape with lower kinetic energy and a shift to higher binding energies would be observed (figure 7, bottom). Upon electron-hole pair recombination, the net charge effect of the positive ions at the surface will become larger than that of the electrons and a total binding energy shift towards higher binding energies is expected. In the steady-state reached under illumination with the laser pulse train (figure 7, bottom panel 4), the shift towards higher binding energies could therefore correspond to cation accumulation towards the surface of the crystal compared to the equilibrium dark state. The slow decay of the photovoltage in the dark corresponds to the slow relaxation of ions back to a neutral charge distribution between crystal surface and bulk (figure 7, bottom panel 5). These screening effects have for example been discussed by Eames *et al* for solar cell devices, where they found iodide vacancies to migrate induced by an electrical field within the perovskite layer, leading to a change in the energy landscape under operation [62]. However, ion movement is not considered in the model described in equation (1). Hence, no recombination time in the dark can be calculated using this model.

Instead, an exponential decay after illumination was found. A time constant of 225 s, corresponding to a rate constant of 4.4×10^{-3} s^{-1}, was determined. In comparison, Wang *et al* biased $MAPbBr_3$ single crystals via silver electrodes and studied ion migration through the current response and found decay times of seconds [54]. Others observed iodide vacancy migration induced via biasing in $MAPbI_3$ multi-crystalline pellets, where the post bias current decay involved two components: a faster, few seconds, decay time and a slower, hundreds of seconds, decay time [63]. Importantly, full recovery was not reached within 10 min [63]. Furthermore, impedance spectra on full perovskite solar cell devices have shown a lower frequency contribution related to ion vacancy migration with RC values in the order of 10–500 mHz, corresponding to 100 s to 2 s, respectively [64]. Others illuminated $MAPbI_xCl_{3-x}$ perovskite solar cells at open circuit voltage, monitored the decay time of the voltage post illumination and found decay times in the order of seconds to 100 s [65, 66]. In other words, slow decays of hundreds of seconds have been observed and linked with ion movement. Overall, our timescale for photovoltage decay in Cs-doped $FAPbI_3$ matches well with time scales for ion migration and diffusion observed by others and these processes are the most likely explanation for the observed binding energy shift.

The time-resolved core level measurements presented here give insight into photovoltages and electric field redistribution between perovskite surfaces and bulk under illumination. By using pump-probe PES and laser ON/OFF measurements, we were able to follow processes in ps to μs and s to min timescales, respectively, which allowed us to distinguish between electron and ion movement causing the photovoltages. Furthermore, using prolonged laser ON versus OFF cycles, we were able to assess the ion mobility of the two crystal compositions relative to one another. This demonstrates the importance of time-resolved

measurements over a wide range of timescales for determining the origin of photovoltages at perovskite surfaces. The use of PES allowed for such investigations at single crystal surfaces enabling us to determine timescales for electron–hole recombination and ion movement intrinsic to the investigated perovskites without the presence of contact layers or grain boundaries in the material.

5. Conclusions

In conclusion, we have successfully carried out TR-PES on two lead halide perovskite surfaces ($CsPbBr_3$, Cs-doped $FAPbI_3$), which give insight into the surface electronic structure and electron and ion dynamics upon illumination through changes in core level binding energies. The two crystals showed different signs of their binding energy shifts under illumination and vastly different dynamics of photovoltage decay. For $CsPbBr_3$, the shift to lower binding energy under illumination and dynamics of recovery of the binding energy indicate downward band bending towards the surface and a photovoltage induced by electron accumulation at the surface, as the dynamics match with electronic processes. The recombination time between surface electrons and holes in the bulk was determined to be 56.3 μs at equilibrium band bending from fitting the photovoltage decay in kinetic traces determined from pump-probe measurements.

For the Cs-doped $FAPbI_3$ surface, a photovoltage decay time constant of 225 s was determined from the change in binding energy observed in the dark after prolonged laser illumination. For this crystal, it was not possible to resolve photovoltage dynamics from pump probe measurements with a laser repetition frequency of 10.4 kHz. Electronic processes alone are therefore unlikely to induce the observed binding energy changes. Instead, we assign the observed dynamics to ion movement and the change in binding energy to positive ion accumulation at the surface under illumination. The mobility of ions under laser exposure in the crystals is further confirmed by prolonged laser ON/OFF measurements, which revealed an increase in cesium and bromide content relative to lead for $CsPbBr_3$ and an increase in iodide and carbon relative to lead for Cs-doped $FAPbI_3$. Higher ion mobility was found for the Cs-doped $FAPbI_3$ surface, which could explain why the photovoltage dynamics are dominated by ion movement for this surface.

Overall, we propose that both crystals show downwards band bending towards the surface under dark conditions. However, for Cs-doped $FAPbI_3$ electron movement towards the surface under illumination is followed by the accumulation of positive ions at the surface causing overall shifts towards higher binding energies. This study highlights the benefit of studying different timescales to time-resolve ionic and electronic dynamics, as electrons and ions move at different timescales. Furthermore, ion rearrangement is often thought to be determined by grain boundaries in thin films. Here, we show that ion rearrangement between the surface and bulk of a single crystal is possible. Our results further show the importance of ion movement on charge dynamics and in that respect also on device behavior, i.e. electron extraction in solar cells may be impacted by ion movement. We further highlighted that different crystal compositions can behave inherently different under illumination despite similar energy alignment in the dark.

Future studies including different laser fluences and sample temperatures could give further insights and allow to model the material's behavior or study different crystal structures and temperature-dependent ion movement, respectively. Additionally, the dependence of ion movement on perovskite composition could be further investigated by studying other compositions such as mixed halide crystals.

Data availability statement

The data cannot be made publicly available upon publication because the cost of preparing, depositing and hosting the data would be prohibitive within the terms of this research project. The data that support the findings of this study are available upon reasonable request from the authors.

Acknowledgment

We thank the Helmholtz-Zentrum Berlin für Materialien und Energie for the allocation of synchrotron radiation beamtime. We thank the Swedish Research Council (Grant Nos. VR 2018-04125, VR 2018-06465, VR 2018-04330, VR 2022-03168 and VR 2023-05072) and the Göran Gustafsson foundation for funding. This work was partially supported by the Wallenberg Initiative Materials Science for Sustainability (WISE) funded by the Knut and Alice Wallenberg Foundation.

ORCID iDs

Birgit Kammlander https://orcid.org/0000-0002-7390-3062
Alberto García-Fernández https://orcid.org/0000-0003-1671-9979

Ute B Cappel https://orcid.org/0000-0002-9432-3112

References

[1] Srivastava A, Satrughna J A K, Tiwari M K, Kanwade A, Yadav S C, Bala K and Shirage P M 2023 Lead metal halide perovskite solar cells: fabrication, advancement strategies, alternatives, and future perspectives *Mater. Today Commun.* **35** 105686
[2] Dong H, Ran C, Gao W, Li M, Xia Y and Huang W 2023 Metal halide perovskite for next-generation optoelectronics: progresses and prospects *eLight* **3** 3
[3] Huang Y, Yu J, Wu Z, Li B and Li M 2024 All-inorganic lead halide perovskites for photocatalysis: a review *RSC Adv.* **14** 4946–65
[4] Zhuang J, Wang J and Yan F 2023 Review on chemical stability of lead halide perovskite solar cells *Nanomicro Lett.* **15** 84
[5] Guo X *et al* 2023 Mitigating surface deficiencies of perovskite single crystals enables efficient solar cells with enhanced moisture and reverse-bias stability *Adv. Funct. Mater.* **33** 2213995
[6] Almasabi K *et al* 2023 Hole-transporting self-assembled monolayer enables efficient single-crystal perovskite solar cells with enhanced stability *ACS Energy Lett.* **8** 950–6
[7] Chen W *et al* 2023 Highly bright and stable single-crystal perovskite light-emitting diodes *Nat. Photon.* **17** 401–7
[8] Hwang I 2023 Challenges in controlling the crystallization pathways and kinetics for highly reproducible solution-processing of metal halide perovskites *J. Phys. Chem.* C **127** 24011–26
[9] Witt C *et al* 2023 Orientation and grain size in $MAPbI_3$ thin films: influence on phase transition, disorder, and defects *J. Phys. Chem.* C **127** 10563–73
[10] Lou Y, Zhang S, Gu Z, Wang N, Wang S, Zhang Y and Song Y 2023 Perovskite single crystals: dimensional control, optoelectronic properties, and applications *Mater. Today* **62** 225–50
[11] Liu C *et al* 2023 Bimolecularly passivated interface enables efficient and stable inverted perovskite solar cells *Science* **382** 810–5
[12] Sun K and Müller-Buschbaum P 2023 Shedding light on the moisture stability of halide perovskite thin films *Energy Technol.* **11** 2201475
[13] Béchu S, Ralaiarisoa M, Etcheberry A and Schulz P 2020 Photoemission spectroscopy characterization of halide perovskites *Adv. Energy Mater.* **10** 1904007
[14] Bröcker D, Gießel T and Widdra W 2004 Charge carrier dynamics at the SiO_2/Si(100) surface: a time-resolved photoemission study with combined laser and synchrotron radiation *Chem. Phys.* **299** 247–51
[15] Zu F, Shin D, Gutierrez-Partida E, Stolterfoht M, Amsalem P and Koch N 2023 Charge selective contacts to metal halide perovskites studied with photoelectron spectroscopy: x-ray, ultraviolet, and visible light induced energy level realignment *Adv. Mater. Interfaces* **10** 2300413
[16] Maheu C, Hellmann T, Prabowo C, Jaegermann W, Hofmann J P and Mayer T 2023 Photoelectron spectroscopy of co-evaporated and spin-coated LiTFSI-doped spiro-OMeTAD reveals the interface energetics inside a MAPI-based perovskite solar cell *J. Phys. Chem.* C **127** 21351–62
[17] Zhang Z and Yates J T 2012 Band bending in semiconductors: chemical and physical consequences at surfaces and interfaces *Chem. Rev.* **112** 5520–51
[18] Stevie F A and Donley C L 2020 Introduction to x-ray photoelectron spectroscopy *J. Vac. Sci. Technol.* A **38** 063204
[19] Teeter G, Harvey S P, Perkins C L, Ramanathan K and Repins I L 2019 Comparative *operando* XPS studies of quasi-Fermi level splitting and open-circuit voltage in CZTSe/CdS and CIGS/CdS junctions and device structures *J. Vac. Sci. Technol.* A **37** 031202
[20] Spencer B F *et al* 2013 Time-resolved surface photovoltage measurements at n-type photovoltaic surfaces: Si(111) and ZnO(100) *Phys. Rev.* B **88** 195301
[21] Zu F, Wolff C M, Ralaiarisoa M, Amsalem P, Neher D and Koch N 2019 Unraveling the electronic properties of lead halide perovskites with surface photovoltage in photoemission studies *ACS Appl. Mater. Interfaces* **11** 21578–83
[22] Amelot D *et al* 2020 Revealing the band structure of FAPI quantum dot film and its interfaces with electron and hole transport layer using time resolved photoemission *J. Phys. Chem.* C **124** 3873–80
[23] Zu F, Amsalem P, Salzmann I, Wang R, Ralaiarisoa M, Kowarik S, Duhm S and Koch N 2017 Impact of white light illumination on the electronic and chemical structures of mixed halide and single crystal perovskites *Adv. Opt. Mater.* **5** 1700139
[24] Bi E, Song Z, Li C, Wu Z and Yan Y 2021 Mitigating ion migration in perovskite solar cells *Trends Chem.* **3** 575–88
[25] Liu Y, Ievlev A V, Borodinov N, Lorenz M, Xiao K, Ahmadi M, Hu B, Kalinin S V and Ovchinnikova O S 2020 Direct observation of photoinduced ion migration in lead halide perovskites *Adv. Funct. Mater.* **31** 2008777
[26] Shao Y *et al* 2016 Grain boundary dominated ion migration in polycrystalline organic–inorganic halide perovskite films *Energy Environ. Sci.* **9** 1752–9
[27] Kim T *et al* 2023 Mapping the pathways of photo-induced ion migration in organic-inorganic hybrid halide perovskites *Nat. Commun.* **14** 1846
[28] Sloboda T *et al* 2020 A method for studying pico to microsecond time-resolved core-level spectroscopy used to investigate electron dynamics in quantum dots *Sci. Rep.* **10** 22438
[29] Giangrisostomi E *et al* 2018 Low dose photoelectron spectroscopy at BESSY II: electronic structure of matter in its native state *J. Electron Spectros. Relat. Phenomena* **224** 68–78
[30] Giangrisostomi E, Ovsyannikov R, Haverkamp R, Sorgenfrei N L A N, Neppl S, Sezen H, Johansson F O L, Svensson S and Föhlisch A 2023 Inhomogeneity of cleaved bulk MoS_2 and compensation of its charge imbalances by room-temperature hydrogen treatment *Adv. Mater. Interfaces* **10** 2300392
[31] Shirley D A 1972 High-resolution x-ray photoemission spectrum of the valence bands of gold *Phys. Rev.* B **5** 4709–14
[32] Powell C J 2020 Practical guide for inelastic mean free paths, effective attenuation lengths, mean escape depths, and information depths in x-ray photoelectron spectroscopy *J. Vac. Sci. Technol.* A **38** 023209
[33] García-Fernández A *et al* 2022 Experimental and theoretical core level and valence band analysis of clean perovskite single crystal surfaces *Small* **18** 2106450
[34] Kammlander B, Svanström S, Kühn D, Johansson F O L, Sinha S, Rensmo H, Fernández A G and Cappel U B 2022 Thermal degradation of lead halide perovskite surfaces *Chem. Commun.* **58** 13523–6
[35] García-Fernández A, Kammlander B, Riva S, Kühn D, Svanström S, Rensmo H and Cappel U B 2023 Interface energy alignment between lead halide perovskite single crystals and TIPS-pentacene *Inorg. Chem.* **62** 15412–20
[36] García-Fernández A, Kammlander B, Riva S, Rensmo H and Cappel U B 2024 Composition dependence of x-ray stability and degradation mechanisms at lead halide perovskite single crystal surfaces *Phys. Chem. Chem. Phys.* **26** 1000–10

[37] Chen L, Yoo J W, Hu M, Lee S and Il Seok S 2022 Intrinsic phase stability and inherent bandgap of formamidinium lead triiodide perovskite single crystals *Angew. Chem.* **134** e202212700
[38] Arya S, Mahajan P, Gupta R, Srivastava R, Kumar Tailor N, Satapathi S, Sumathi R R, Datt R and Gupta V 2020 A comprehensive review on synthesis and applications of single crystal perovskite halides *Prog. Solid State Chem.* **60** 100286
[39] Mannino G, Deretzis I, Smecca E, La Magna A, Alberti A, Ceratti D and Cahen D 2020 Temperature-dependent optical band gap in $CsPbBr_3$, $MAPbBr_3$, and $FAPbBr_3$ single crystals *J. Phys. Chem. Lett.* **11** 2490–6
[40] Hua Y *et al* 2024 Suppressed ion migration for high-performance x-ray detectors based on atmosphere-controlled EFG-grown perovskite $CsPbBr_3$ single crystals *Nat. Photon.* **18** 870–7
[41] Hieulle J, Son D, Jamshaid A, Meng X, Stecker C, Ohmann R, Liu Z, Ono L K and Qi Y 2022 Metal halide perovskite surfaces with mixed A-site cations: atomic structure and device stability *Adv. Funct. Mater.* **33** 2211097
[42] Shin D, Zu F, Cohen A V, Yi Y, Kronik L and Koch N 2021 Mechanism and timescales of reversible p-doping of methylammonium lead triiodide by oxygen *Adv. Mater.* **33** 2100211
[43] Schulz P, Cahen D and Kahn A 2019 Halide perovskites: is it all about the interfaces? *Chem. Rev.* **119** 3349–417
[44] Dong S, Hu Z, Wei P, Han J, Wang Z, Liu J, Su B, Zhao D and Liu Y 2022 All-inorganic perovskite single-crystal photoelectric anisotropy *Adv. Mater.* **34** 2204342
[45] Sloboda T, Kammlander B, Berggren E, Riva S, Giangrisostomi E, Ovsyannikov R, Rensmo H, Lindblad A and Cappel U B 2024 Interface-resolved photovoltage generation dynamics and band structure evolution in a PbS quantum dot solar cell *Nanoscale* **16** 21002–10
[46] Polishchuk S *et al* 2022 Nanoscale-resolved surface-to-bulk electron transport in $CsPbBr_3$ perovskite *Nano Lett.* **22** 1067–74
[47] Cappel U B *et al* 2017 Partially reversible photoinduced chemical changes in a mixed-ion perovskite material for solar cells *ACS Appl. Mater. Interfaces* **9** 34970–8
[48] Svanström S, Jacobsson T J, Sloboda T, Giangrisostomi E, Ovsyannikov R, Rensmo H and Cappel U B 2018 Effect of halide ratio and Cs^+ addition on the photochemical stability of lead halide perovskites *J. Mater. Chem.* A **6** 22134–44
[49] Svanström S, García Fernández A, Sloboda T, Jacobsson T J, Rensmo H and Cappel U B 2021 X-ray stability and degradation mechanism of lead halide perovskites and lead halides *Phys. Chem. Chem. Phys.* **23** 12479–89
[50] Donakowski A, Miller D W, Anderson N C, Ruth A, Sanehira E M, Berry J J, Irwin M D, Rockett A and Steirer K X 2021 Improving photostability of cesium-doped formamidinium lead triiodide perovskite *ACS Energy Lett.* **6** 574–80
[51] Li J, Han Z, Gu Y, Yu D, Liu J, Hu D, Xu X and Zeng H 2020 Perovskite single crystals: synthesis, optoelectronic properties, and application *Adv. Funct. Mater.* **31** 2008684
[52] Chen L, Wang H, Zhang W, Li F, Wang Z, Wang X, Shao Y and Shao J 2022 Surface passivation of $MAPbBr_3$ perovskite single crystals to suppress ion migration and enhance photoelectronic performance *ACS Appl. Mater. Interfaces* **14** 10917–26
[53] Wang X *et al* 2020 Ion migrations in lead halide perovskite single crystals with different halide components *Phys. Status Solidi* b **257** 1900784
[54] Wang W, Wang X, Zhang B, Guo Y and Xu Q 2020 Ion migration of $MAPbBr_3$ single crystal devices with coplanar and sandwich electrode structures *Physica* B **593** 412310
[55] Lim J, Kober-Czerny M, Lin Y-H, Ball J M, Sakai N, Duijnstee E A, Hong M J, Labram J G, Wenger B and Snaith H J 2022 Long-range charge carrier mobility in metal halide perovskite thin-films and single crystals via transient photo-conductivity *Nat. Commun.* **13** 4201
[56] Woo Y W, Jung Y-K, Kim G Y, Kim S and Walsh A 2022 Factors influencing halide vacancy transport in perovskite solar cells *Discov. Mater.* **2** 8
[57] Staub F, Hempel H, Hebig J-C, Mock J, Paetzold U W, Rau U, Unold T and Kirchartz T 2016 Beyond bulk lifetimes: insights into lead halide perovskite films from time-resolved photoluminescence *Phys. Rev. Appl.* **6** 044017
[58] Sridharan A, Noel N K, Hwang H, Hafezian S, Rand B P and Kéna-Cohen S 2019 Time-resolved imaging of carrier transport in halide perovskite thin films and evidence for nondiffusive transport *Phys. Rev. Mater.* **3** 125403
[59] He Y *et al* 2018 High spectral resolution of gamma-rays at room temperature by perovskite $CsPbBr_3$ single crystals *Nat. Commun.* **9** 1609
[60] Rong S-S, Faheem M B and Li Y-B 2021 Perovskite single crystals: synthesis, properties, and applications *J. Electron. Sci. Technol.* **19** 100081
[61] Battula R K, Sudakar C, Bhyrappa P, Veerappan G and Ramasamy E 2022 Single-crystal hybrid lead halide perovskites: growth, properties, and device integration for solar cell application *Cryst. Growth Des.* **22** 6338–62
[62] Eames C, Frost J M, Barnes P R F, O'Regan B C, Walsh A and Islam M S 2015 Ionic transport in hybrid lead iodide perovskite solar cells *Nat. Commun.* **6** 7497
[63] García-Batlle M, Deumel S, Huerdler J E, Tedde S F, Guerrero A, Almora O and Garcia-Belmonte G 2021 Mobile ion-driven modulation of electronic conductivity explains long-timescale electrical response in lead iodide perovskite thick pellets *ACS Appl. Mater. Interfaces* **13** 35617–24
[64] Clarke W, Richardson G and Cameron P 2024 Understanding the full zoo of perovskite solar cell impedance spectra with the standard drift-diffusion model *Adv. Energy Mater.* **14** 2400955
[65] Pockett A, Eperon G E, Sakai N, Snaith H J, Peter L M and Cameron P J 2017 Microseconds, milliseconds and seconds: deconvoluting the dynamic behaviour of planar perovskite solar cells *Phys. Chem. Chem. Phys.* **19** 5959–70
[66] Pockett A, Eperon G E, Peltola T, Snaith H J, Walker A, Peter L M and Cameron P J 2015 Characterization of planar lead halide perovskite solar cells by impedance spectroscopy, open-circuit photovoltage decay, and intensity-modulated photovoltage/photocurrent spectroscopy *J. Phys. Chem.* C **119** 3456–65